Session 4

Bildverarbeitung & -analyse

Multi-Level Approach for the Discriminative Generalized Hough Transform

H. Ruppertshofen [1,2], D. Künne [1], C. Lorenz [3], S. Schmidt [4,2], P. Beyerlein [4], Z. Salah [2], G. Rose [2], H. Schramm [1]

[1] University of Applied Sciences Kiel, Institute of Applied Computer Science, Kiel, Germany
[2] Otto-von-Guericke University, Institute of Electronics, Signal Processing and Communication Technology, Magdeburg, Germany
[3] Philips Research Laboratories, Hamburg, Germany
[4] University of Applied Sciences Wildau, Department of Engineering, Wildau, Germany

Contact: heike.ruppertshofen@fh-kiel.de

Abstract:

The Discriminative Generalized Hough Transform (DGHT) is a method for object localization, which combines the standard Generalized Hough Transform (GHT) with a discriminative training technique. In this setup the aim of the discriminative training is to equip the models used in the GHT with individual model point weights such that the localization error in the GHT becomes minimal. In this paper we introduce an extension of the DGHT using a multi-level approach to improve localization accuracy and to reduce processing time. The approach searches for the target object on multiple resolution levels and combines this information for better and faster results. The advantage of the approach is demonstrated on whole-body MR images, which are intended for PET attenuation correction.

Keywords: Object Localization, Generalized Hough Transform, Machine Learning, Discriminative Training, Multi-level Approach

1 Problem

In the area of radiation therapy planning or computer-assisted interventions and diagnosis, object localization is a prerequisite for many applications in medical image processing, e.g., segmentation algorithms, where an initial position of the segmentation model in the image needs to be known. In many applications this step is still performed manually or specialized solutions are developed for each individual problem [1]. In order to obtain fully automatic processing chains, automatic and general algorithms need to be developed, which can localize objects of arbitrary shape.
Recently, we have proposed a general algorithm for object localization, called Discriminative Generalized Hough Transform (DGHT) [2], which combines the Generalized Hough Transform (GHT) [3] with a discriminative training algorithm. The procedure runs fully automatic and is independent of the target object, which is searched for in the image. The only restriction for the target is that it should be well defined by its shape. For the medical localization tasks considered by us, our algorithm achieves high quality results, mainly tested on 2D images [2]. Until now the GHT has been applied only rarely to 3D images due to its computational complexity [4]. Nevertheless, we have shown in [5] that the application of our algorithm to 3D images becomes practicable due to sparse models and the restriction of transformation parameters, i.e. estimating only translation.
However, when the region of the target object exhibits only low contrast or when many similar objects are visible in the image, the localization is hampered. Furthermore, if the images are large and high localization accuracy is needed, the feasibility of the procedure is questioned due to long processing times. To solve these issues, we introduce an extension of the DGHT using a multi-level approach for more robust and faster results. The target object is first searched for on a low resolution image and the result of this search is used as input for the next higher resolution level, meanwhile reducing the size of the search region.
The extension of the algorithm is tested on whole-body MR images, which were acquired for a PET attenuation correction [5]. Since patients often have to undergo several subsequent MR examinations, fast acquisitions and low specific absorption rates (SAR) are of higher interest for this task than a detailed mapping of the anatomy. The resulting image resolution, resembling the resolution of PET, is rather low, which complicates the image processing due to the lack of anatomical detail available, but also renders it very interesting for the proposed algorithm.

2 Methods and Material

The GHT [3] is a standard method for object localization, which employs a point model to represent and search for a target object in an image. The model is thereby moved across the edge image corresponding to the original image and the co-incidences of model and edge points are counted in a voting process and accumulated in the Hough space. The Hough cell, which obtained the highest vote, is assumed to represent the true target location.
In the DGHT the models are furthermore equipped with individual model point weights. These weights are trained with a discriminative training algorithm [6], based on the information available in the Hough space, i.e. which point has voted in which Hough cell, with the aim to obtain a low localization error in the GHT.
In order to obtain a meaningful model and to be able to capture the variability contained in a training dataset, the model for the GHT is generated directly from the image data by taking the edge points from a given volume of interest (VOI) around the target point from a number of images and is refined in an iterative approach. The procedure starts on a small set of training images, on which preliminary model point weights are trained. The current model is then evaluated on a larger development dataset. Images where the model performs poorly are added to the training dataset, further model points are created from these images, and another iteration is performed until the error on all development images is below a certain threshold or no further improvement is achieved. For more detailed information on the iterative training technique and the DGHT, we refer the reader to [2].
In this paper, we introduce the combination of the DGHT with a multi-level approach. To this end, a Gaussian pyramid of the image is created and the localization is performed on each level. To speed up the procedure the localization is first executed on the lowest resolution level, where only little detail is visible and the localization is fast, due to the small image size. For the next higher resolution level it is assumed that the previous localization result is near the target point such that the search can be constrained to a smaller region. In the following experiments an extract with half the side lengths of the previously considered image extract is cut out around the localized point, such that the number of pixels remains almost constant, while the resolution of the image increases. Thus more and more detail is taken into account on each level while zooming into the target object. The idea of the approach is illustrated in Fig. 1.
For each level of the pyramid an individual model is created using edge points from a VOI as stated above. While the VOI needs to be given for the standard approach, here it is chosen to be centered at the target point with a side length of 75% of the current image extract. Only part of the extract is used for model generation in order to reduce model size and to prevent the algorithm from learning the exact field of views, which might be different on test images.

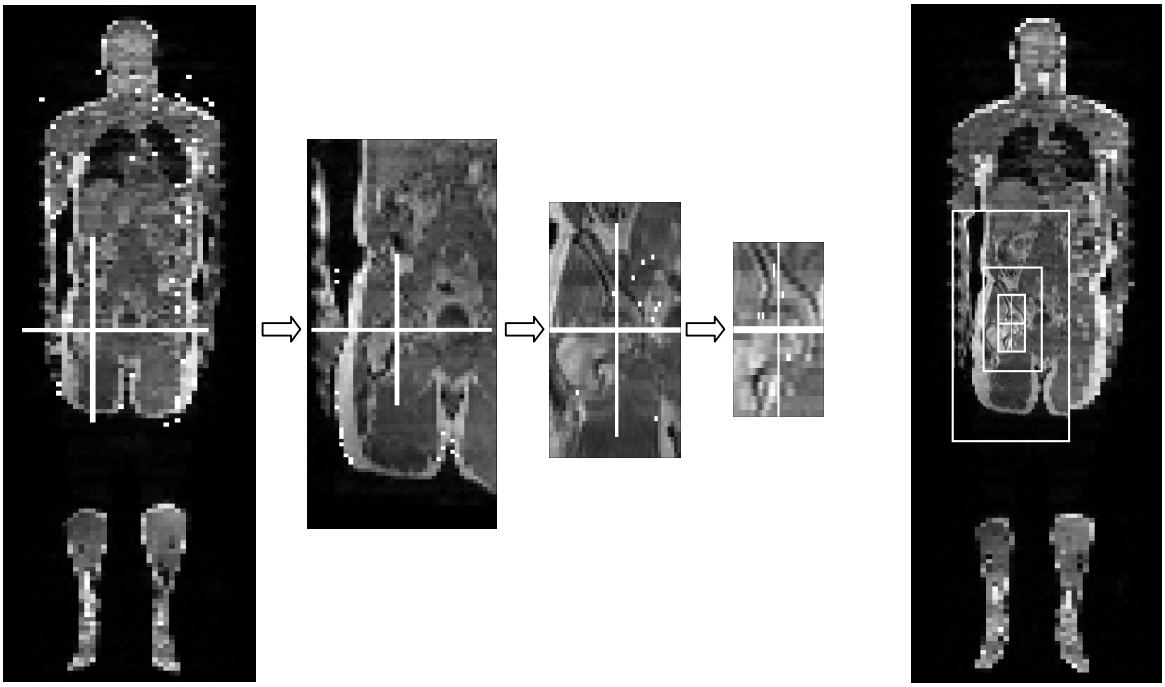

Fig. 1: Illustration of the steps of the multi-level approach. The localization procedure starts on the low resolution image on the left. In the subsequent steps (left to right), the procedure zooms into the target by performing the localization on regions with decreasing size and increasing resolution around the previously localized point (white cross hairs). The right image shows an overlay of the different image extracts used for the localization.

The method is tested on 22 whole-body MR images, which were acquired on a Philips Achieva 3T X-Series MRI system using a whole-body protocol suitable for attenuation correction. As was said earlier, the images are not intended for diagnostic purposes but for the attenuation correction of PET images; therefore a sequence with fast acquisition is applied, which results in images with the rather low resolution of approximately 1.875 mm in plane and a slice thickness of 6 mm. Example images are displayed in Fig. 2.
The given task for these images is to localize the femur for a subsequent segmentation. To this end the center of the femoral head of the right leg was chosen as target point, which is marked in the left images in Fig. 2.

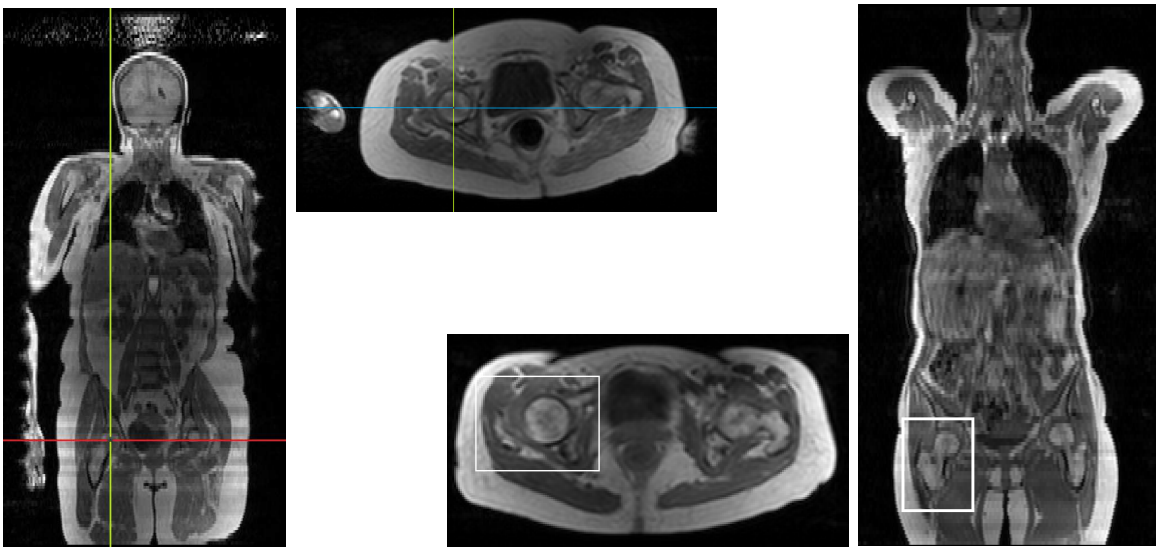

Fig. 2: Coronal and transversal view of two example images. The images on the left additionally show the target point in the center of the femoral head, while the right images display the VOI, which was used for model generation in the standard approach.

From the dataset 10 images are chosen randomly as development dataset, while the remaining images are used for testing purposes. The image pyramid is created with 4 levels and since the resolution in z-direction is much larger than in-slice, the image is downsampled only in x- and y-direction for the first levels of the pyramid to obtain a rather isotropic resolution.
To be able to compare the new multi-level approach with the former approach, a second experiment is performed using the same parameter setting. Yet, instead of utilizing an image pyramid, only one resolution level is employed. To reduce processing time and memory need of the GHT, the image is downsampled once in-slice. For the model creation a VOI around the femoral head is defined, which can be seen in Fig. 2 (right).

3 Results

The results of the two experiments are stated in Table 1. For the training images the results differ only slightly with a good mean localization error of 3.1 mm and 2.2 mm for the standard and multi-level approach, which is not surprising since the models were trained on these images. However, regarding the unknown test data, the standard approach was substantially outperformed by the multi-level approach. The latter achieves a much better localization error with a mean distance of 3.8 mm of the localized and annotated point, while the former obtains only 6.7 mm and even fails on one of the test images.

	Training		Test		
	Local. rate	Mean error	Local. rate	Mean error	Proc. time
Standard approach	100 %	3.1 mm	91.6 %	6.7 mm	28 s
Multi-level approach	100 %	2.2 mm	100 %	3.8 mm	3 s

Table 1: Comparison of the two localization approaches. The table states the localization rate and mean error of the correct localizations on the training and unknown test data and the localization time for the two approaches.

The advantage of the multi-level approach becomes even more obvious when considering the processing time. Due to the much smaller image extracts (only 1-3 % of the pixels of the original image) on which the localization is performed on each resolution level, the multi-level approach takes only about 10 % of the processing time of the standard approach.

4 Discussion

The multi-level approach has proven to be significantly better and faster than the standard approach for the given task. The main reason for the smaller localization error is the higher resolution used in the multi-level approach. While the standard approach, due to computational reasons, performs the localization only on the second resolution level of the image pyramid, the multi-level approach employs the original resolution in its final stage. The obtained localization error of 3.8 mm is exceptional, considering the low resolution of the images, especially the slice distance of 6 mm.
Another advantage of the newly proposed approach, which zooms into the target object, is that it takes the neighborhood of the target into account on a larger scale and thereby facilitates to localize objects with low contrast, high variability or which can be easily confused with further objects visible in the image. One of the test images has a smaller field of view compared to the rest of the dataset. This image covers the body only from the head to the upper part of the femur, still showing the femoral head but not the remainder of the femoral bone. The standard approach, which relies on the whole bone being visible, fails to deal with this occlusion, while the multi-level approach, which orients itself on a larger scale, is not affected by the limited field of view.
In the presented example the algorithm achieved to localize the target with the necessary accuracy on all resolution levels. However, if necessary, it would be conceivable to keep several candidate points on each level, which could be discarded later on higher resolution levels, when identified as false-positives.
Besides facilitating the object localization and making it more robust, the multi-level approach has another large advantage, which lies in the shorter processing times. Since the image extracts, which are used for the localization, are much smaller than the original image, only a fraction of the run time is needed, depending on the size of the image and the number of zoom levels used. In the presented example, a reduction of processing time of 10 % was achieved. With the runtime of 3 s the application of the algorithm in 3D becomes really feasible. Furthermore, the procedure is not yet optimized for speed, so that a further reduction of processing time is to be expected.
In future work, the usage of the demonstrated localization procedure in combination with the segmentation for the attenuation correction will be examined. Since only little anatomical detail is visible in the image, a precise positioning of the segmentation models is needed, which we are confident to fulfill with the presented approach.

5 Acknowledgments

The authors would like to thank the Department of Radiology, Mt. Sinai School of Medicine, New York, the Department of Imaging Sciences and Medical Informatics, Geneva University Hospital and the Business Unit NM/CT, Philips Healthcare for providing the data used in this study. This work is partly funded by the Innovation Foundation Schleswig-Holstein under the grant 2008-40 H.

6 References

[1] T. Heimann, B. van Ginneken, M. Styner et al., Comparison and Evaluation of Methods for Liver Segmentation from CT Datasets, IEEE Transactions on Medical Imaging 28(8), 2009
[2] H. Ruppertshofen, C. Lorenz, S. Schmidt, P. Beyerlein, Z. Salah, G. Rose, H. Schramm, Discriminative Generalized Hough Transform for Localization of Joints in the lower extremities, Computer Science – Research & Development 26, Springer, 2011
[3] D. H. Ballard, Generalizing the Hough Transform to Detect Arbitrary Shapes, Pattern Recognition 13(2), 1981
[4] H. Schramm, O. Ecabert, J. Peters, V. Philomin, J. Weese, Towards Fully Automatic Object Detection and Segmentation, Proceedings of SPIE medical imaging, 2006
[4] H. Ruppertshofen, C. Lorenz, S. Schmidt, P. Beyerlein, Z. Salah, G. Rose, H. Schramm, Lokalisierung der Leber mittels einer Diskriminativen Generalisierten Hough Transformation, Proceedings of CURAC, 2010
[5] Z. Hu, N. Ojha, S. Renisch, et al., MR-based Attenuation Correction for a Whole-body Sequential PET/MR System, Proceedings of IEEE Nuclear Science Symposium, 2009
[6] P. Beyerlein, Discriminative Model Combination, Proceedings of IEEE International Conference on Acoustics, Speech and Signal Processing, 1998

Robust and Intuitive Meshing of Bone-Implant Compounds

M. Kahnt[1], F. Galloway[2], H. Seim[1], H. Lamecker[1], M. Taylor[2], S. Zachow[1]

[1] Medical Planning Group, Zuse-Institute Berlin, Germany
[2] Bioengineering Sciences Research Group, School of Engineering Sciences, University of Southhampton, UK

Contact: kahnt@zib.de

Abstract:

To preoperatively assess the functional outcome of a total joint replacement, finite element analysis can be used for an objective evaluation of individual implant configurations. For large scale studies, where the implant configuration is varied in size, position or design, numerous finite element meshes have to be generated. To improve the planning process we propose a method that outputs a merged tetrahedral mesh of the patient's joint anatomy and an arbitrarily positioned implant geometry suitable for finite element analysis. Our approach has several advantages: (1) it avoids error-prone intermediate stages, e.g. data type conversion, (2) it is able to preserve constraints such as sharp edges and (3) it can be fully automated by initially defining a few parameters that describe the desired geometric accuracy and element quality. Based on the meshing of 100 different patient-specific bone-implant setups at the tibia (shinbone), we show that our approach produces high-quality meshes in all cases automatically.

Keywords: orthopedics, finite element analysis, 3d mesh generation, multi-material

1 Motivation

Finite element analysis (FEA) has become an approved instrument in orthopedic surgery to preoperatively assess the functional outcome of joint replacement procedures as it allows for an objective evaluation of bone-implant compounds. When optimizing implant size and position for a single subject or when investigating new implant designs for a large population [1], numerous different implantation setups have to be analyzed to determine and compare characteristics like the expected strains and stresses during everyday activities. To perform such analyses, FE-meshes (typically tetrahedral grids) have to be automatically generated that minimize computation time while maintaining reasonable accuracy of the FEA outcome. In other words, the resulting meshes have to be accurate w.r.t. the patient's anatomy and the implant shape, must be of FE-suitable quality, and consist of as few as possible number of elements [2].

To generate finite element meshes in a joint replacement scenario the input is typically given as a combined description of the subject-specific bone, provided as a geometry or a voxel representation, and the positioned implant that is usually given as a geometry. From those overlapping bone and implant structures, the output is aimed to be a conformal multi-material mesh, i.e. a set of tetrahedra, each of which is assigned to one material and two neighbouring tetrahedra share exactly one of their respective faces (Fig. 1).

Current approaches to generate such tetrahedral meshes typically require an explicit fusion of the objects to be discretized before meshing, for instance using a single voxel- or surface-representation. While inconsistencies resulting from object overlaps are resolved easily within a voxel grid, the resulting mesh typically suffers from artificially introduced inaccuracies, for example lost information about sharp edges [3]. Alternatively, a consistent description as a surface triangulation that separates the different objects (or domains) can be computed. This is likely to cause problems where boundary intersections introduce small angles or narrow inter-boundary regions occur. A triangulation of those regions leads to very small or badly shaped triangles (Fig. 2a). If a meshing approach is used that depends on this boundary representation, like the advancing front method, unnecessarily small or badly shaped finite elements will be introduced.

Recently, Pons et al. [4] introduced a meshing approach, where a so called *oracle* is employed during the mesh generation procedure. At each phase of the meshing process the *oracle* can perform a query to retrieve the current object (or material) at an arbitrary point in 3D space, thus providing an implicit representation of each possible input type, like voxel representations, implicit surfaces or triangular surfaces. This approach allows for a direct meshing without an intermediate generation of a single (explicit) domain description, i.e. no Boolean operations are necessary before the actual volume meshing. The parameters that are set for the volume mesher are the only constraints that guide and restrict the meshing process. However, the *oracle* does not allow for an explicit definition of features to be preserved, like sharp edges (Fig. 2b). In scenarios where the geometry of an object has to be preserved as accurately as possible without introducing too many finite elements, as for mechanical parts like a prosthesis, this might turn out as a significant drawback.

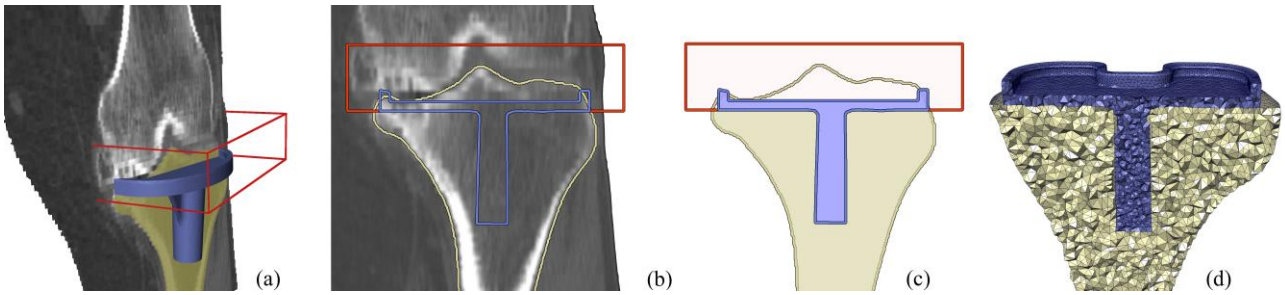

Fig. 1: Meshing setup. (a) Segmented tibial bone (yellow) with aligned implant (blue) and the region where bone will be cut off (red box), (b) 2D view of the setup, (c) overlaps are resolved: the implant covers all other objects, bone within the red box is removed (d) conformal tetrahedral grid.

Contribution We extended the approach of Pons et al. [4] by a method that is specifically designed to handle the above mentioned problem, but still preserves the general concept of the *oracle* approach. Additional geometric constraints can be defined to preserve relevant features at specific locations in the mesh. Furthermore, we provide a hierarchical management of the input objects to intuitively handle their overlaps, e.g. between implant and bone (Fig. 1c). By comparing the results of our new meshing approach to 100 meshed tibiae from a large scale study on biomechanical behaviour [1] we can show that our feature preserving method is able to automatically generate good finite element meshes in terms of element quality.

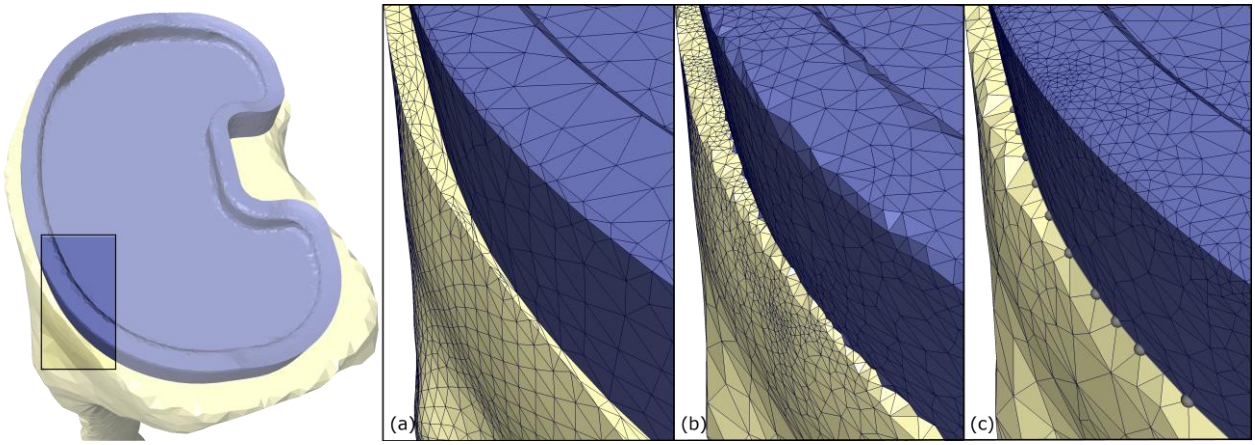

Fig. 2: Meshed bone/implant compound with a narrow region between bone and implant surface. (a) Close-up view of surface-based method; badly shaped or very small triangles are created. (b) Result of the *oracle*-based method without prescribed features, elements have good shape but sharp features are poorly resolved. (c) Close-up view of *oracle*-based method with our feature preserving extension applied to the implant. While sharp edges of the implant have been maintained, the shape of the bone is approximated by the mesher according to desired element size and shape.

2 Methods

The method introduced by Pons et al. [4] is based on refining an initial Delaunay triangulation of randomly selected boundary points, i.e. points that lie on material interfaces. Successive insertions of points locally refine the mesh and are used to adjust the tetrahedralization to the prescribed quality criteria. During the refinement, lists are maintained that contain all *bad* surface triangles (called facets) and all *bad* tetrahedra, i.e. elements that do not fulfill the desired quality criteria. First the algorithm aims at clearing the list of bad facets by adding more interface points in their proximity. As a second step the bad tetrahedra are refined by adding their circumcenter to the point set. This can introduce new bad facets that have to be removed from the facet list before continuing the refinement of the tetrahedra. The algorithm terminates when the mesh contains no more bad facets and tetrahedra, i.e. all quality criteria are fulfilled. The method lacks a criteria for one-dimensional characteristics such as edges and ridges as they appear on mechanical objects like implants. Such features are only represented implicitly by the *oracle* and are being recovered by refinement of the facets according to their quality criteria only. The actual edge is unlikely to be discovered exactly and sharp edges are smoothed out in the final mesh (Fig. 2b).

To explicitly maintain such features, we extended the existing method by another list containing all segments that are prescribed by the user but do not appear in the current meshing stage. The first priority is to maintain those segments before refining any facets and tetrahedra. Analogously to the original method, point insertions for facets and tetrahedra can cause further refinements of the prescribed segments. Boltcheva et al. [5] proposed a similar extension to preserve one-dimensional features for medical image data. Their approach includes an extraction of such features from a single voxel image but does not allow for an adaptive refinement of these edges to assure that the desired quality criteria are met.
To handle overlaps of bone and implant, we implemented a hierarchical model that assigns a priority to each object according to its position in the input list. During the meshing process each point query to the *oracle* automatically returns the material with the highest priority. This allows for an intuitive combination of multiple overlapping objects into a single compound representation. The implant, which should be completely preserved, receives the highest priority. Its vicinity, where bone will be removed, has mid-level priority. Overlaps of this region and lower priority objects will be treated as empty (Fig. 1b). Note that this is different from meshing it beforehand and removing the corresponding material afterwards as this would affect the mesh generation process. In our implant case, bone material with lowest priority will only be meshed in areas where no object with higher priority is located.
The actual meshing method is driven by Delaunay refinement minimizing the overall radius-edge ratio (quotient of radius of the circumsphere and minimal edge length). This ideally leads to meshes that do not contain tetrahedra with very small dihedral angles, because these are mostly induced by elements with at least one short edge but a large circumsphere radius. Small dihedral angles cause an increase of the FE's stiffness matrix' condition and therefore slow down the FE computation or even significantly distort the computational outcome [6]. Delaunay refinement tends to generate so-called slivers that consist of four equally spaced vertices roughly around a circle, exhibiting a small *radius-edge ratio* but also small dihedral angles. To remove slivers, we employ post-processing steps proposed by Cheng et al. [7] and Tournois et al. [8] that locally change the mesh in order to increase the minimal dihedral angle (MDA). We implemented our approach as an extension to the existing 3D Mesh Generation package available in CGAL (version 3.7) [9].

3 Results

From a previous study, FE meshes of implanted tibiae were available that were meshed by an advancing-front approach to compute strains at the bone-implant interface [1]. We randomly selected one hundred virtual total knee replacement settings from that study, including geometric representations of the tibia and the tibial component. For each implant the region where protruding bone is removed was given and its sharp edges were marked as line segments to be preserved. Note that edge features had to be defined only once and could also be computed automatically by a feature extraction algorithm [10]. The one hundred datasets were then meshed with and without our feature-preserving extension, where the latter essentially equals the original method by Pons et al. [4]. In both setups the desired quality criteria were chosen as follows: (1) a maximal *radius-edge ratio* of 1.1 for all materials, (2) a maximal *cell size* (circumsphere radius) of 1mm for the implant and 3 mm for the bone and (3) a maximal *facet distance* of 0.1 mm to approximate the surfaces for the implant and 2 mm for the bone material. While meshing failed in 7 cases with the previous method due to distorted elements, all meshes were generated successfully with our new approach.
The FE-meshes generated with our feature preservation enabled met the quality criteria with 437,000 tetrahedra on average (range 295,000 to 707,992). The number of tetrahedra generated without feature preservation was significantly larger with an average number of 900,898 tetrahedra per mesh (range 614,234 to 1,533,011).
During FEA the condition of the stiffness matrix plays a crucial role for the efficiency of finite element analysis. This property is closely related to the worst tetrahedral element of the grid in terms of the minimal dihedral angle [6]. For the new meshes, generated including feature preservation, the average MDA was 8.72° (±1.31°). The models that where generated using an advancing front approach and used for FEA [1] obtained an average MDA of 4.09° (±3.18°) (Fig. 3).

4 Discussion

We introduced a new method to automatically generate tetrahedral meshes of bone-implant compounds from any configuration of implant and bone suitable for FEA (Fig. 2 and 4). In contrast to state-of-the-art methods, our approach does not require the error-prone generation of intermediate representations to resolve overlaps of the objects to be meshed. Instead a hierarchy on these objects implicitly represents the compound. Features like sharp edges can be predefined to explicitly maintain such geometric properties if necessary. The desired mesh quality is guided by only a few parameters. The quality of the generated meshes and the possibility to fully automate the meshing process make our new method an ideal tool for FEA on a large amount of meshing configurations or clinical implementations of FEA-based decision support systems in orthopedic surgery and beyond.

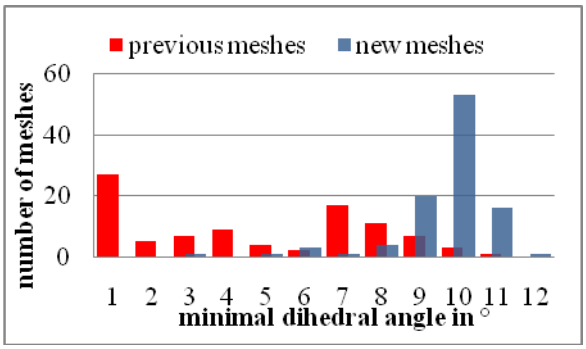

Fig. 3: Minimal dihedral angles (MDA) of all 100 meshed bone-implant compounds. A large number of models meshed with the previous method has very small MDAs. With our new approach only a few models exhibit MDAs below 5 degrees.

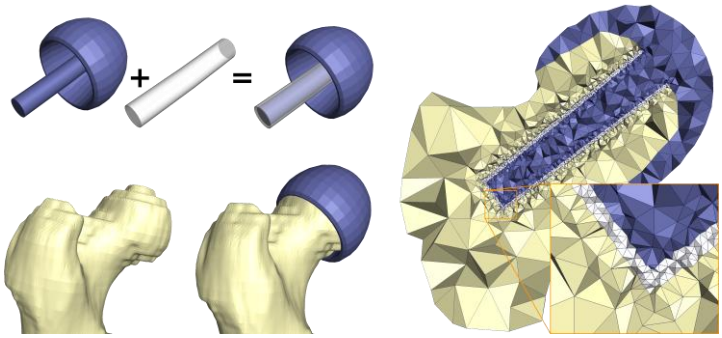

Fig. 4: Example implantation setup for a hip resurfacing (proximal femur). A cement layer surrounds the implant's stem. Bone will be removed were it interferes with the implant.

With our feature preserving extension we obtain significantly fewer tetrahedral elements compared to the original method using identical quality criteria. We attribute this to the fact that for the original method geometric accuracy (mainly guided by the facet distance) is achieved by further *unguided* refinement of the mesh in areas where the quality criteria are not met. Our method specifically aims at reconstructing the requested features first due to a more targeted point insertion during the refinement process in those areas. The minimal dihedral angle (MDA) of the new meshes (with feature preservation) is significantly larger than the MDA obtained with an advancing front approach we used to generate FE-meshes for a large scale study. This is an important indicator that the models generated with our method are suitable for FEA. Proving termination of our extended Delaunay refinement method is subject to future work as well as investigating the influence of our new approach on the FEA in terms of convergence time and simulation outcome.

Acknowledgments This work was partially supported by the EU-FP7 Project MXL (ICT-2009.5.2) and the DFG Research Center Matheon.

5 References

[1] Galloway F, Kahnt M, Seim H, et al. A large scale finite element study of an osseointegrated cementless tibial tray. In: *23th Annual Symposium International Society for Technology in Arthroplasty*.; 2010.

[2] Lamecker H, Mansi T, Relan J, et al. Adaptive Tetrahedral Meshing for Personalized Cardiac Simulations.In: *CI2BM09 - MICCAI Workshop on Cardiovascular Interventional Imaging and Biophysical Modelling*.; 2009:149-158.

[3] Zachow S, Zilske M, Hege H-Chr. 3D Reconstruction of Individual Anatomy from Medical Image Data: Segmentation and Geometry Processing. In: *25. ANSYS Conference & CADFEM Users' Meeting, Dresden.; 2007*

[4] Pons J, Ségonne F, Boissonnat J, et al. High-quality consistent meshing of multi-label datasets. In: *Information Processing in Medical Imaging*.; 2007:198–210.

[5] Boltcheva D, Yvinec M, Boissonnat J-D. Feature preserving Delaunay mesh generation from 3D multi-material images. *Computer Graphics Forum*.; 2009:1455-1464.

[6] Shewchuk JR. What Is a Good Linear Finite Element? Interpolation, Conditioning, Anisotropy, and Quality Measures. In: *Proceedings of the 11th International Meshing Roundtable*.; 2002:115 - 126.

[7] Cheng S-W, Dey TK, Edelsbrunner H, Facello MA, Teng S-H. Sliver exudation. *Journal of the ACM*.; 2000:883-904.

[8] Tournois J, Srinivasan R, Alliez P. Perturbing slivers in 3D Delaunay meshes. In: *Proceedings of the 18th International Meshing Roundtable*.; 2009

[9] CGAL: Computational Geometry Algorithms Library. Available at: http://www.cgal.org.

[10] Hildebrandt K, Polthier K. Smooth feature lines on surface meshes. In: *Proceedings of the third Eurographics symposium on Geometry processing (SGP)*.; 2005:85.

Phantom-based evaluation of a semi-automatic segmentation algorithm for cerebral vascular structures in 3D ultrasound angiography (3D USA)

C. Chalopin[1], K. Krissian[2], A. Müns[3], F. Arlt[3], J. Meixensberger[3], D. Lindner[3]

[1] Universität Leipzig, ICCAS, Leipzig, Germany
[2] Universidad de Las Palmas de Gran Canaria, GIMET, Las Palmas, Spain
[3] Universität Leipzig, Klinik für Neurochirurgie, Leipzig, Germany

Kontakt: claire.chalopin@iccas.de

Abstract:

Intraoperative ultrasound angiography (USA) provides to the neurosurgeon real-time information about the cerebral vascular network but is difficult to interpret due to the presence of noise and artifacts. A segmentation algorithm may improve the visualization of data by extracting the vascular structures only. We propose to adapt and test an existing model-based segmentation method on 3D USA data of a vascular phantom with 4 mm tube radii. The performance of the algorithm is evaluated by comparison with a gold standard (CT data) and with manual delineations. The algorithm generated a segmentation model whose radii values are overestimated of more than half of one mm in comparison with the gold standard but with more realistic geometrical features than the manual delineations.

Keywords: 3D ultrasound angiography, vascular segmentation, physical phantom

1 Problem

Intraoperative ultrasound angiography (iUSA) is an imaging modality which, in neurosurgery, enables the surgeon to visualize the real-time information of the anatomy and function of the cerebral vascular network during the intervention [1]. With the development of new ultrasound contrast agents, contrast harmonic imaging (CHI) is becoming an emerging modality, which enables enhancing the main cerebral vascular structures in the images. However, the interpretation of iUSA data may be complex. The image quality is reduced by the speckle, but also by the presence of blood and cerebrospinal liquids which occur during the surgical intervention. The contrast agent induces artifacts as well, called bubble noise and blooming effect. Boundaries of the vascular structures are therefore unclearly defined in the USA data. The extraction of the vascular structures would improve their visualization by keeping the object of interest only and by eliminating noise and artifacts.

Segmentation of vascular structures has already been extensively studied and validated with success on patient data but mainly focuses on good quality images [2]. Some methods have been however adapted on US data. In 3D power Doppler data thresholding techniques ([3]) or region growing algorithms ([4]) are the most common methods used. In 3D B-mode volumes model-based techniques are required to overcome the problem of unclear borders. Two dimensional active contours performing slice by slice ([5]) and a dynamic balloon represented by a triangular mesh ([6]) have been used to segment the carotid contours. Furthermore, Krissian et al [6] proposed a model-based multiscale scheme that computes a vesselness measure to segment the aorta artery. The model is represented by a circular cross-section cylinder. The technique aims estimating the centerline position and radii values of elongated structures in the data. A multiscale implementation allows extracting vascular structures of different sizes. It is then possible to generate a segmentation model from the estimated centerlines and radii values. None of these methods have been validated so far on 3D USA data of the brain.

In this work we aim to quantitatively estimate on a physical vascular phantom the performance of an adapted version of the semi-automatic segmentation method proposed in [6].

2 Methods

Semi-automatic segmentation method

The segmentation method is based on a model-based multiscale detection of the vessel centerlines using a cylindrical model with circular cross-section. Briefly, a vesselness measure is computed for each voxel of the USA volume which represents the probability that a voxel belongs to the centerline of an elongated structure. The vesselness measure at a voxel position is computed based on the image gradient information along a circle C which centre is the voxel itself. Its orientation is defined based on the computation of the eigenvectors of the structure tensor which represent the directions of axis and cross-section of the elongated structure. The structure tensor is computed for a sigma value σ proportional to the radius value r of the elongated structure, representing the radius value of the circle C. Thus, a multi-scale implementation consisting in computing the vesselness measures for N_{scales} different radii values $r_{lower} \leq r \leq r_{upper}$ is used to extract vascular structures of various sizes. For each voxel, the maximum vesselness response is kept in the multiscale space and the corresponding r_{max} value represents an estimation of the radius. In the original method, the user manually selects the vascular structure centerlines in the volume of maximum vesselness responses. In order to reduce the interaction, the maximum vesselness responses are here thresholded with a value $T_{maxvess}$ provided by the user. The centerline segments whose sizes are shorter than a given pruning size $S_{pruning}$ are considered as noise and are automatically eliminated. A surface reconstruction of the vascular structures, called here segmentation model, is then generated based on the extracted centerlines and estimated radii information. The surface is obtained in two steps: i) creation of a volume data representing the distance transform to the estimated tubular structures processing each segment as a circular cylinder, ii) iso-surface generation based on the marching cubes algorithm (Figure 2a).

Physical vascular phantom and 3D US acquisition

The physical phantom includes two silicon tubes mimicking blood vessels whose inside diameter is 4 mm and wall thickness is 1 mm (Figure 1a). The silicon tubes have been laid down into a plastic container filled with gelatine. The acquisition system of the 3D USA data includes a common US device (Sonoline Elegra, Siemens) with a 2D free-hand 2.5 MHz phased array probe, an optical tracking system (NDI, Polaris) and a navigation system (SonoNavigator, Localite). The optical tracking system aims at estimating the position of the US probe in the room. The navigation system is used to compound the set of 2D US images acquired with the US probe within an US volume. The vascular phantom is linked to a pump which simulates a laminar blood flow within the tubes, filled with water. Short before the acquisition, an US contrast agent (SonoVue, Bracco) is injected into the phantom tubes. The operator scans then the phantom surface with the US probe positioned perpendicular to the tube lengths and moved parallel to the tubes. A set of 2D enhanced images is obtained and sent to the navigation system through a S-video connection. A 3D USA volume of voxel size $1\times1\times1$ mm^3 is eventually reconstructed (Figure 1 b and c).

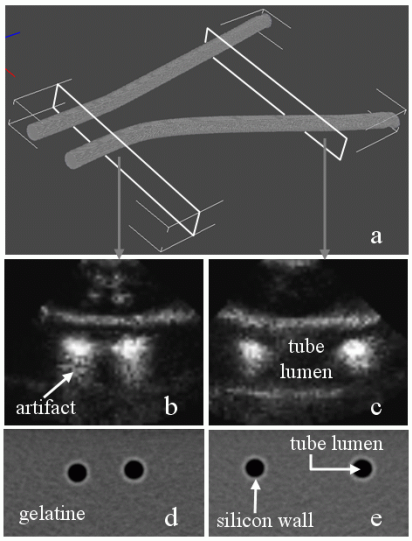

Figure 1: The physical vascular phantom includes two silicon tubes mimicking the blood vessels (a). (b) and (c) are two slices of the 3D USA data acquired with an US contrast agent. (d) and (e) are two slices of the CT volume.

Evaluation of the segmentation algorithm by comparison with a gold standard

We assume that the phantom tube geometrical features may deform during the building (weight of the gelatine) and through the image acquisition process (pressure of the US probe on the phantom surface). We estimate therefore the performance of the segmentation algorithm operating on the 3D USA data by comparison with CT data of the phantom, considered as gold standard. A CT scanner (Philips) is used here in helical mode with 0.33 mm spacing between the slices. The pixel size in the slices is 0.20x0.20 mm². The phantom tubes are filled with water and the scanning performed without the pump for easier practical reasons (Figure 1 d and e).

The extraction of tube lumens in the CT data is performed by a region growing algorithm with upper threshold value set to zero representing the interface between the silicon wall and the water (Figure 2b). Evaluation of the segmentation algorithm performance is done by comparing the tube lumen radii values. As it was already described above, the model-based segmentation algorithm provides an estimate of the radii values for each point of the extracted centerlines. The radii values in the CT data are computed as following. We assume, based on visual observation, that the tube lumens are perpendicular to volume cross-sections, and that therefore the lumen cross-sections are disks. The number of voxels included in the lumen cross-sections is counted in each volume cross-section. It represents the surface S_{CT} and the radii values r_{CT} are then deduced.

Comparison of the segmentation algorithm and manual delineations

Result of the segmentation algorithm is then compared to manual delineations. Seven observers manually delineated the tube lumen borders in the 3D USA data of the phantom using the free ITK-SNAP segmentation tool. The observers needed between 15 to 30 minutes to perform the task. High differences between the manual delineations are observed and the delineation of two observers has been removed due to a too large overestimation of the tube lumens. An average volume has been then computed from the manual delineations of the five remaining observers (Figure 2c).

The geometrical features defined for the comparison are the tube lumen cross-section area and the centerline distance, since the lumen contours in the average delineation are rather elliptic. The cross-section areas are computed for each volume cross-section as the number of lumen voxels. The average delineation has been thinned to extract the lumen centerline and the distance to the centerline of the segmentation model computed for each volume cross-section.

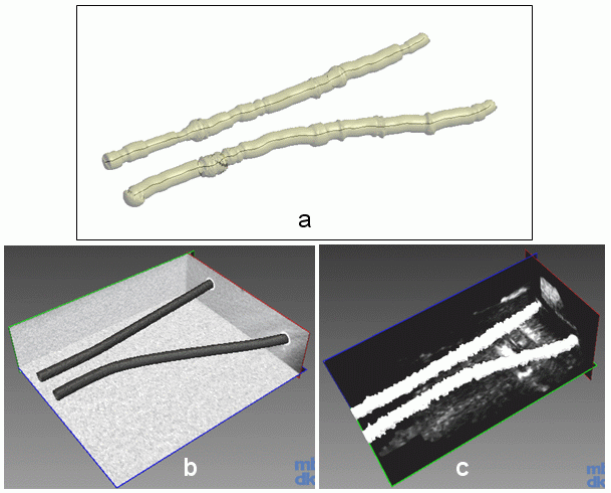

Figure 2: Phantom tube lumens extracted by (a) the segmentation algorithm in the 3D USA data, (b) a region growing method in the CT data and (c) manual delineations performed in the 3D USA data by observers and averaged.

3 Results

Segmentation model generation

The tube lumens have been segmented in the 3D USA data using the segmentation method previously described. Although the known dimensions of the silicon tubes in the phantom are constant, the tube lumen diameters do not look homogeneous in the 3D USA data. The segmentation algorithm has been therefore applied in a multi-scale manner with

the following values: r_{lower}=0.5, r_{upper}=5.0 and N_{scales}=10. Thus, a large set of radii values are tested by the algorithm. The segmentation model has been generated with $T_{maxvess}$=15.0 and $S_{pruning}$=5 (Figure 2a).

Comparison of the segmentation model with the gold standard and the average delineation

Geometrical features have been calculated on the segmentation model, the gold standard and the average delineation as previously explained. Since the voxel size is different in both volumes, the mean values and standard deviations have been used for the comparison (Table 1). Values show that the mean radii values in the segmentation model are larger than nearly one millimeter in comparison to the real tube lumen size and larger than more than half of a millimeter in comparison to the gold standard. The mean cross-section areas estimated by the observers are twice larger than those values in the gold standard although this report is smaller than two in the comparison between the segmentation model and the gold standard. The mean centerline distance values calculated between the segmentation model and the mean delineation is less than one voxel (0.8 ± 0.6 mm for tube 1 and 0.6 ± 0.6 mm for tube 2). The tube centerlines are therefore estimated nearly at the same position by the algorithm and the observers.

	radii values (mm)		cross-section area (mm^2)	
	tube 1	tube 2	tube 1	tube 2
phantom	2.0	2.0	12.6	12.6
gold standard	2.24 ± 0.04	2.30 ± 0.05	15.8 ± 0.6	16.5 ± 0.7
average delineation	-	-	41.6 ± 6.8	38.6 ± 5.2
segmentation model	2.80 ± 0.43	3.03 ± 0.38	30.0 ± 5.8	25.9 ± 7.2

Table 1: Comparison of the segmentation model with the gold standard and the average delineation using the radii and cross-section area features.

4 Discussion

Comparison results showed that the mean radius value of the segmentation model generated by the algorithm is overestimated of more than half of a millimeter in comparison with the gold standard. Two main reasons may explain this difference. First, the image resolution in the US data is lower, increasing the partial volume effect. The tube lumen diameters look visually larger than 4 voxels. Second, the tube lumen cross-sections in the US data look rather like an ellipse, due to the US probe pressure during the data acquisition. Visually, the circular cross-sections of the segmentation model have for radii values the largest ellipse axis. Moreover the geometrical features calculated in the gold standard are slightly larger than the real tube sizes meaning that the phantom deformed. We showed moreover that the observers still more overestimated the tube lumen cross-section area than the segmentation algorithm did it. They have been more hindered by noise and artifacts in the data to correctly delineate the unclear tube borders. We conclude that the segmentation algorithm succeeded therefore, on our vascular phantom, in providing a model with realistic geometrical features regarding the low image resolution of the 3D USA data and in eliminating noise and artifacts. Moreover, processing time for the multi-scale scheme was less than one minute for a volume of 62x71x145 voxels. The algorithm parameters r_{lower}, r_{upper}, N_{scales} and $S_{pruning}$ may be set fixed, also for patient data. Only the threshold value $T_{maxvess}$ for extracting the vascular structures has to be tuned since its value is a compromise between the among of information and the among of noise in the segmentation model. However, the segmentation tool is suitable for the operating room.

Next step will consist in evaluating the segmentation algorithm on a more realistic vascular phantom including tubes of different radii values and close to the cerebral vascular anatomy and with bifurcations. It should be interesting to check the behavior of the segmentation algorithm on thinner tubes and bifurcations. Tests on intraoperative 3D USA data of patients is planed as well since the goal of the project is to integrate the segmentation model of the intraoperative cerebral vascular network into a navigation system. Applications might be the guidance of the neurosurgeon to reach the tumor without damaging the surrounding blood vessels or the check of the success of aneurysm clipping surgeries.

5 References

[1] Unsgaard G, Rygh OM, Selbekk T, Müller TB, Kolstad F, Lindseth F, Nagelhus Hernes TA. Intra-operative 3D ultrasound in neurosurgery. Acta Neurochir 2006;148:235-253.

[2] Kirbas C, Quek Francis. A review of vessel extraction techniques and algorithms. ACM Computing Surveys 2004;36(2):81-121.

[3] Reinertsen I, Lindseth F, Unsgaard G, Collins DL. Clinical validation of vessel-based registration for correction of brain-shift. Medical Image Analysis 2007;11:673-684.

[4] Hold S, Hensel K, Winter S, Dekomien C, Schmitz G. Segmentation of blood vessels in 3D ultrasound-datasets by a model-based region growing algorithm In Proceedings of Computer Assisted Orthopaedic Surgery (CAOS) 2007:610-603.

[5] Gill J, Ladak H, Steinman D, Fenster A. Accuracy and Variability Assessment of Semi-Automatic Technique for Segmentation of the Carotid Arteries from 3D Ultrasound Images. Medical Physics 2000;27(6):1333-1342.

[6] A Zahalka, A Fenster. An automated segmentation method for three-dimensional carotid ultrasound images. Phys Med Biol 2001;46:1321-1342.

[7] Krissian K, Ellsmere J, Vosburgh K, Kikinis R, Westin CF. Multiscale segmentation of the aorta in 3D ultrasound images. Proceedings of the 25th Annual Int. Conf. on the IEEE Engineering in Medicine and Biology Society, EMBS, Cancun Mexico 2003:638-641.

Different approaches to volume assessment of lymph nodes in CT Scans of HNSCC in comparison with a real gold standard

S.Mueller[1], A. Boehm[1], G. Wichmann[3], L. Dornheim[4], P.Stumpp[2], J. Bertollini[5], B. Preim[4], A. Dietz[1]

1 Department of ENT and plastic surgery, University Hospital of Leipzig, Liebigstr. 10-14, 04103 Leipzig, Germany
2 Department of diagnostic and interventional Radiology, University Hospital Leipzig, Liebigstr. 18, 04103 Leipzig, Germany
3 ENT Research Laboratory, Medical Faculty, University of Leipzig, Liebigstr. 21, 04103 Leipzig, Germany
4 University of Magdeburg - Visualization Group
5 Institute of Pathology, University Hospital Leipzig, Liebigstr. 26, 04103 Leipzig, Germany

Kontakt: stefan.mueller2@medizin.uni-leipzig.de

Abstract:
Objectives:
Volume assessment in head and neck squamous cell carcinoma (HNSCC) becomes an increasing important clinical parameter in treatment planning and response control. Various authors showed a significant impact of tumor volume on outcome and local control. In this study we compared the "gold standard", the diameter based approach, with segmentation based approaches
Methods:
The segmentations were based on CT scans of 4 patients with HNSCC undergoing neck dissection as part of their treatment. These scans were taken during staging and a total of 20 lymph nodes were segmented. They were selected by size and location close to reproducible anatomical structures. The true volumes were measured by water displacement.
Results:
Pearson's correlation index shows a higher correlation of the diameter generated volumes (r=0.723) than results generated via segmentation (r=0.527) with the true volumes. Nonetheless diameter generated volumes show clearly too high volumes at 146.8% (Confidence Interval: 115.8% – 186.1%). Volumes generated with the segmentation are at 116.5% (Confidence Interval: 93.9% – 144.7%).
Conclusions:
The data show a higher reliability of volumes estimated by the segmentation based approach than the widely used diameter based approach.

Keywords: Tumor Volume, Segmentation, DeLOS , Response, HNSCC

Purpose

The entity of head and neck squamos cell cancer (HNSCC) is showing a worldwide clearly rising incidence [1]. It was shown, that the existence of lymph node metastasis in HNSCC has a significant impact on the survival rate [2]. The 5 year survival rate of patients with HNSCC without nodal metastasis is 73%, dropping to 50% in case of positive nodes without extra capsular spread and even further down to 30% in case of extra capsular spread. The overall survival rate of patients in Europe is 40% and has remained unchanged in the years 1983 until 1994 according to the WHO [1].

In the past years tumor volume investigations have become a subject of increasing interest. The improved quality of radiological images, last but not least due to thin sliced spiral computed tomography (CT) scans, as well as post processing of these pictures have made the volume determination from these sources possible [15]. The general impact of tumor volume on treatment outcome has been shown in various studies [3,4,5,6,7,13]. Some authors also propose a recognition of tumor volume estimations in the TNM staging systems [14,6]. Unfortunately there are no widely used systems or methods with the necessary reliability for tumor volume measurement in HNSCC. Following the lack of such a system there is also no standard in volume assessment.
At the moment it is common practice to follow up lesion extensions as described by the RECIST criteria [8]. Here the largest diameters of initially chosen lesions are being compared along the treatment. Graser et al. could show a higher grade of accuracy for the perimeter based method in comparison to the RECIST criteria [9]. Sorensen et al. [10] could show that the interreader and intrareader variability could be reduced with the perimeter method, hence suggesting that

a higher accuracy in response measurement can be achieved. Based on a performed literature review in pubmed we couldn't find any studies to directly compare the preoperatively determined volume with the real volume of the excised specimen.
The aim of this study therefore is to compare the real volume of a lesion as obtained by using a real gold standard with volume data gained by the diameter based method as well as with perimeter based method. Based on the rising number of studies on primary conservative treatment, like the GermanDeLOS II study, new treatment and outcome monitoring tools should be developed - such focusing on the increasing hardware and software capabilities.

Methods
After completion of the necessary staging examinations and after the histological confirmed tumor diagnosis, the indication for surgical treatment including neck dissection was set by an experienced consultant. This treatment option was discussed, specified and agreed in the tumor board. In all included cases, the surgical procedure applied included at least one neck dissection as part of the overall treatment. Based on the CT scans, two segmentation approaches were performed to facilitate planning of the surgical treatment by selective neck dissection and allowed to make comparison of the data with the real volumes (see below).
After obtaining informed consent from the patient, potential lymph nodes in the CT scans of the neck were selected to perform the investigations. These scans were part of the preliminary staging examinations, so that there was no additional exposure to radiation.
The lymph nodes included in the study have been selected due to their location close to surgical and anatomical landmarks. Such was done to help the surgeon with intra operative recognition of the specific lymph nodes. One criterion for the selected lymph nodes was that they were suspect to be potentially local metastases and that they therefore were part of the anyway removed nodes. This assured avoidance of any unnecessarily performed additional surgical intervention. Another criterion was the size of the nodes included in this study. Taking into account that there is – due to the partial volume effect – an increasing inaccuracy by decreasing size [11], we specifically selected small lymph nodes below 1 cm of maximum diameter. The segmentation was done with the newly developed software "NeckSegmenter". This software was developed by the visualization group at the University of Magdeburg.
With the assistance of an experienced head and neck radiologist, measurements were obtained by outlining the lymph nodes in each slice. In addition, segmentation of the landmark structures on the neck was performed. The landmark structures segmented included the sternocleidomastoid muscle, the common, internal and external carotid artery, the jugular and facial veins, the hyoid bone, the thyroid cartilage, the cricoids cartilage as well as the major branches of the carotid arteries. For higher accuracy reasons there was no interpolation performed during segmentation. Following the outlining process, the datasets were used to generate a 3D model of the lymph node by the second software called the "Tumor Therapy Manager". Here the virtual volume could be measured and the structures were visualized.

For comparison with the actual standard in volume assessment, the diameter based method, the three largest orthogonal diameters in every lesion were measured in the same dataset. The volume was then computed by using the formula for standard sphere volume:

$$V = 1/6\ \pi\ (a * b * c) \qquad (1)$$

During surgery, the surgeon had access to the 3D reconstruction of the patient neck to identify the selected lymph nodes. After identification and resection, the nodes were put in a transport medium and were brought directly to the laboratory. Any leftover surrounding connective tissue was removed by leaving the node capsule intact. After drying of the nodes we performed a volume measurement by using the water displacement method – according to Archimedes principle. In a previous work it could be shown that this is an accurate method for volume determination especially in irregular shaped and small objects [12].
The displaced volume was assessed using calibrated pipettes (Pipetman; Gilson, Inc., Middleton, WI). Additionally, the displaced water and as well the lymph nodes were weighed by use of Mettler's AJ150 (Mettler-Toledo GmbH, Gießen), an analytical microbalance (d=0.1 mg, e=1.0 mg) calibrated by the *Sächsische Landesamt für Mess- und Eichwesen* (validity until 2013).
Following this process the lymph nodes were further investigated and processed immediately by the department of pathology, and the results were integrated into the final pathological report for the patient.

Results
We analyzed the 20 lymph nodes of four patients with local metastases of their HNSCC. All patients were males, and their mean age was 57 years. Two of the patients underwent surgery because of oropharyngeal cancer of the tonsil, the others suffered from carcinoma of the larynx. After completion of the histological analysis two lymph nodes of the study specimens showed metastasis of the previously diagnosed carcinomas, while the other 18 lymph nodes were his-

tological free of metastasis. We initially selected 27 nodes in the diagnostic CT Scans. Seven of the segmented lymph nodes had to be removed from the final data set, since they could not be reliable detected and exactly localized and hence safely matched between CT scan and the surgical situs without doubt. The 20 remaining lymph nodes that were properly confirmed could be used for further analysis (see table 1).

Table 1 Characteristics of the HNSCC included in the study

Patient	Sex	TNM	Localization	Lymph Nodes analyzed [n]
1	M	pT 2 pN0 cM0	Oropharynx	5
2	M	pT 2 pN1 cM0	Oropharynx	6
3	M	pT4a pN2c cM0	Larynx	5
4	M	ypT1 pN2b cM0	Larynx	4

To compare the obtained results, the Pearson product-moment correlation coefficient (r) was used. This coefficient showed a higher correlation of the diameter generated volumes (r=0.723) than perimeter generated results (r=0.527) with the true volumes. Further analysis of the data showed a systematic over estimation of true volumes by the diameter generated volumes leading to a mean overestimation of about 50% (mean=146.8%; CI: 115.8%-186.61%). In comparison to that the mean volume difference between the true volumes and the perimeter based volumes was at 116.6% (Confidence Interval: 93.9% – 144.7%).

Conclusion:

The results presented show a higher reliability for the perimeter based volumes, although Pearson's *r* showed a higher correlation for the diameter based volume. Use of diameter-based volume assessment poses the risk of faulty interpretation of imaging data due to its systematic tendency of overestimation. This makes the diameter-based approach vulnerable and potentially can cause wrong treatment follow up. Contrary, the perimeter based approach shows values closer to the true volumes. However, in interpretation of the presented data one should take into account the relatively small size and therefore the even stronger impact of the partial volume effect. From our point of view, these results show the need for further studies and bigger sample sizes. Thus aiming last but not least to define clear levels of trust for different lesions and their extensions as well as providing new segmentation algorithms with a realistic test setup.

References:

1. Peter Boyle, Bernhard Levin (2008) Cancer Site by Site. In WHO World Cancer Report. WHO Press, Geneva, 330-336
2. Jochen A. Werner, Anja A. Duenne, Jeffrey N. Myers (2003) Functional anatomy of the lymphatic drainage system of the upper aerodigestive tract and its role in metastasis of squamous cell carcinoma. Head & Neck 25:322-332
3. Christopher R. Johnson, Howard D. Thames, David T. Huang, Ruppert K. Schmidt-Ulrich(1995) The influence of quantitative tumor volume measurements on local control in advanced head and neck cancer using concomitant boost accelerated superfractionated irradiation. Int. J. Radiation Oncology Biol. Phys., 32:635-641
4. Wai-Man Sze, Anne W.M. Lee, Tsz-Kok Yau, Rebecca M.W. Yeung, Kam-Ying Lau et al. (2004) Primary tumor volume of nasopharyngeal carcinoma: Prognostic significance for local control. Int. J. Radiation Oncology Biol. Phys., 59:21-27
5. Daniel T.T. Chua, Jonathan S.T. Sham, Dora L.W. Kwong, K.S. Tai, P.M. Wu et al. (1997) Volumetric analysis of tumor extent in nasopharyngeal carcinoma and correlation with treatment outcome. Int. J. Radiation Oncology Biol. Phys., 39:711-719
6. Vincent F.H. Chong (2007) Tumour volume measurement in head and neck cancer. Cancer Imaging 7, S47-49
7. Johnson CR. Thames HD, Huang DT, et al. (1995) The tumor volume and clonogen number relationship: tumor control predictions based upon tumor volume estimates derived from computed tomography. Int. J. Radiation Oncology Biol. Phys., 33: 281-7
8. E.A. Eisenhauer, P. Therasse, J. Bogaerts, L.H. Schwartz, D. Sargent, R. Ford et al. (2009) New response evaluation criteria in solid tumours: Revised RECIST guideline (version 1.1). Europ. J. of Cancer 45 228 –247
9. A. Graser, CR Becker, MF Reiser, C. Stief, M. Staehler (2008) Volumetry of metastases from renal cell carcinoma: comparison with the RECIST criteria. Radiologe 48(9):850-6
10. A. Gregory Sorensen, Shveta Patel, Carla Harmath, Sarah Bridges, Jennifer Synnott et al. (2001) Comparison of diameter and perimeter methods for tumor volume calculation. J. Clin Oncol 19:551-557
11. J. Rexilius, H. K. Hahn, H. Bourquain, HO. Peitgen (2003) Ground Truth in MS Lesion Volumetry – A Phantom Study. Medical Image Computing and Computer-Assisted Intervention - MICCAI 2003 Lecture Notes in Computer Science, 2003, Volume 2879/2003, 546-553

12. Stephen W. Hughes (2005) Archimedes revisited: a faster, better, cheaper method of accurately measuring the volume of small objects. Physics Education 40, 468-474
13. M.K. Chen, T.H. Chen, J.P. Liu et al. (2004) Better prediction of prognosis for patients with nasopharyngeal carcinoma using primary tumor volume. Cancer 100: 2160-6
14. Hadi R, Kumar S, Srivastava M, Pant M C, Srivastava P K, Jamal N (2010): Quantitative Tumor Volume VS TNM Staging: The Impact on Prognosis in Head and Neck Cancer. The gulf journal of oncology 8
15. M. Fischer, G. Straus,S. Gahr, I. Richter et al. (2009) Three-dimensional visualization for preoperative planning and evaluation in head and neck surgery. Laryngorhinootologie;88(4):229-33